Transport of Magma in Granitic Mush Systems; an Example From the Götemar Pluton, Sweden

Mattsson, Tobias; McCarthy, William; Schmiedel, Tobias

DOI
10.1029/2023GC011061

Publication date
2024

Document Version
Final published version

Published in
Geochemistry, Geophysics, Geosystems

Geochemistry, Geophysics, Geosystems®

AGU ADVANCING EARTH AND SPACE SCIENCES

RESEARCH ARTICLE
10.1029/2023GC011061

Transport of Magma in Granitic Mush Systems; an Example From the Götemar Pluton, Sweden

Tobias Mattsson[1,2], William McCarthy[2], and Tobias Schmiedel[3,4]

[1]Department of Geological Sciences, Stockholm University, Stockholm, Sweden, [2]School of Earth and Environmental Sciences, University of St. Andrews, St. Andrews, UK, [3]Department of Earth Sciences, Uppsala University, Uppsala, Sweden, [4]Department of Geoscience & Engineering, TU Delft, Delft, The Netherlands

Key Points:

- Subhorizontal magma transport in a granitic magma mush controlled by magma emplacement structures
- Vertical magma sheets in granitic magma mush controlled by the regional stress field
- Magma transported in concentric magma fingers in the circular Götemar granite pluton

Supporting Information:

Supporting Information may be found in the online version of this article.

Correspondence to:

T. Mattsson,
tobias.mattsson@geo.su.se

Citation:

Mattsson, T., McCarthy, W., & Schmiedel, T. (2024). Transport of magma in granitic mush systems; an example from the Götemar pluton, Sweden. *Geochemistry, Geophysics, Geosystems*, *25*, e2023GC011061. https://doi.org/10.1029/2023GC011061

Received 23 MAY 2023
Accepted 19 DEC 2023

Author Contributions:

Conceptualization: Tobias Mattsson
Formal analysis: Tobias Mattsson, William McCarthy
Funding acquisition: Tobias Mattsson
Investigation: Tobias Mattsson, William McCarthy, Tobias Schmiedel
Methodology: Tobias Mattsson, William McCarthy
Project Administration: Tobias Mattsson
Resources: Tobias Mattsson, William McCarthy
Validation: Tobias Mattsson
Visualization: Tobias Mattsson

Abstract Granitic magma bodies form in the ephemeral part of magma mush systems and are emplaced by a variety of mechanisms in different tectonic settings. This study investigates how granitic magma emplacement processes and tectonomagmatic interactions assert control over the architecture of mush state pluton-scale magma transport pathways. The 1.45 Ga shallow-crustal Götemar pluton is a 4.5 km diameter circular pluton that consists of three granite units: a coarse-grained red granite, a medium-grained pale to red granite, and fine-grained pale microgranite sheets. We employed geological mapping supported by Anisotropy of Magnetic Susceptibility (AMS) to examine the magmatic and regional tectonic controls on late-stage magma transport in the Götemar granitic magma mush system. Multiple parallel arcuate subhorizontal microgranite and medium-grained granite sheets (from 0.1 to 10s of meters thick) were mapped within the pluton. The arcuate sheets pinch out from the northern part of the pluton toward the SE inferring magma propagation direction. A dominant set of vertical granitic sheets within the granite body strikes NW-SE. The AMS fabrics are contact-parallel in the main medium-grained granite body and indicate inflation. Within the microgranite sheets, the AMS fabrics are parallel to the sheet strike and support a sheet propagation direction to the SE. The Götemar pluton displays a clear link between arcuate (concentric) magma-transporting sheets and concentric strain-partitioning related to the intrusion of medium-grained granite magma. The vertical magma sheet orientations are consistent with an NE-SW extensional stress field that is associated with the extensional back-arc stress regime of the contemporary Hallandian Orogen.

Plain Language Summary The eruptive products of volcanoes are thought to be stored in pockets of melt in crystal-dominated magmatic systems called crystal mushes prior to volcanic eruptions. An understanding of where magma is stored and how it is transported in mush systems is important in order to predict the eruptive behavior of the volcanic system. This contribution investigates the magma transport pathways in the Götemar granite in Sweden and its relationship to local magmatic deformation and regional deformation related to the Hallandian mountain building event. We show that magma is transported in vertical sheets parallel to the front of the Hallandian Orogen and laterally in sub-horizontal arcuate sheets that reflect the circular shape of the granite pluton. Our study highlights the importance of understanding the shape and the formation of the magmatic granite body for deciphering the melt transport in the magma mush system under volcanoes.

1. Introduction

Magmatic systems dominated by crystalline material, so-called crystal mushes, are commonly suggested to grow by the stacking of sills fed by vertical dikes (Cashman et al., 2017; Jackson et al., 2018). In relation to magmatic mush systems, granitic magma bodies are considered to represent the short-lived, peripheral, or ephemeral parts of the mush where melt accumulates before potential volcanic eruptions (Glazner, 2021; Hildebrand et al., 2010). Granitic plutonic magma bodies can be emplaced by a variety of mechanisms, such as, but not limited to, laccolith type-doming, trap-door deflection of the roof, wall deflection, roof uplift or floor subsidence accommodated by faults, floor sagging, cantilever floor subsidence and magma sheeting (Burchardt et al., 2012; Cruden, 1998; Cruden & McCaffrey, 2001; Gilbert, 1877; Hawkes & Hawkes, 1933; Hutton, 1988; Mattsson et al., 2020; McCarthy, Petronis, et al., 2015; Miller & Paterson, 2001; Paterson & Fowler, 1993; Pollard & Johnson, 1973; Richey, 1928). In addition, the mode of granitic magma emplacement is often linked to the contemporary regional tectonic stress field and deformation (Hutton, 1988; Jacques & Reavy, 1994; McCarthy, Reavy, et al., 2015; Miller & Paterson, 2001; Olivier et al., 2016; Petronis et al., 2012; Reichardt & Weinberg, 2012; Vigneresse, 1995;

Writing – original draft: Tobias Mattsson, William McCarthy, Tobias Schmiedel
Writing – review & editing: Tobias Mattsson, William McCarthy, Tobias Schmiedel

Weinberg et al., 2004). However, it is unclear if melt is transported and accumulated in tabular stacked sills in mushy granite magma bodies irrespective of tectonic setting and pluton emplacement mechanism. This study investigates if the factors controlling magma body emplacement, including the ambient tectonic stress field, also affect magma transport within a granitic plutonic magma body in a mushy state. We employ geological mapping supported by Anisotropy of Magnetic Susceptibility (AMS) on the Götemar granite pluton to provide insights into factors controlling magma transport within a crystal mush. When we use the term magma or crystal mush in the text we refer to a solid where melt occurs in the interstices of the crystal framework (see Weinberg et al., 2021).

2. Geological Setting

The 1.45 Ga Götemar pluton is a circular (4.5 km in diameter) granitic pluton located in southeastern Sweden that intruded steeply foliated 1.84 to 1.77 Ga granites and granodiorites of the Transscandinavian Igneous Belt (Åhäll, 2001; Cruden, 2008; Kresten & Chyssler, 1976; Ripa & Stephens, 2020; Wik et al., 2005). The mapped exposure of the Götemar pluton has an area of 18.2 km^2. Gravimetric measurements suggest that the Götemar pluton has a vertical extent of 4 km and a maximum horizontal extent of 10 km below the current exposure level and its emplacement depth has been estimated to be between 4 and 8 km (Cruden, 2008). The Götemar pluton forms part of an NNE-SSW trending line of Mesoproterozoic plutons and circular aeromagnetic anomalies in the Baltic Sea that have been proposed to mark a back-arc rift zone to the contemporary Hallandian/Danopolonian orogenic event (Bogdanova et al., 2001; Brander & Söderlund, 2009; Cruden, 2008; Ripa & Stephens, 2020; Söderlund et al., 2008; Ulmius et al., 2015; Wik et al., 2005) (Figure 1a).

The Götemar pluton consists of three major granite units: (a) a coarse-grained red granite that surrounds an (b) medium-grained pale to red granite, and subhorizontal to steeply dipping (c) pale, aphyric to porphyritic microgranite sheets (Figures 2 and 3a–3c) (Friese et al., 2012; Kresten & Chyssler, 1976). Sheets of granite also occur in the host rock within 100–300 m of the Götemar pluton (Kresten & Chyssler, 1976). All granite units are most readily distinguished based on texture and are composed of quartz, alkali feldspar, plagioclase, muscovite, and minor biotite, fluorite and zircon (Friese et al., 2012). The coarse-grained granite records high-temperature healed crystal deformation, multiple generations of quartz crystals, and metasomatic quartz replacement of feldspar and mica, which are proposed to be related to the intrusion of magma pulses into a granitic mush (Friese et al., 2012). The intrusion of the Götemar pluton was also associated with host rock greisen formation and hydrothermal veining (Tillberg et al., 2019).

The Götemar pluton is cut by multiple regional faults with up to 500 m of estimated vertical displacement and minimal lateral offset (Kresten & Chyssler, 1976) (Figure 1b). Several curved deformation zones occur within the pluton, which are defined by topographical troughs and wetlands that are parallel to the pluton-host rock contact (Figure 1b). Three cores were previously drilled in the Götemar granite pluton to assess rock quality at potential sites for radioactive waste disposal (Scherman, 1978) (see Figure 2 for core locations). Cores C1 and C2 were drilled vertically, whereas C3 was drilled at an inclination of 50° to the North. In the first 506 m long core (C1), 4 microgranite sheets ranging from 0.5 to 6.3 m in thickness were intersected. In the second (C2) 602 m long core, 25 microgranite sheets were intersected with sheet thicknesses ranging from 0.3 to 23 m with an average thickness of 3.1 m. In the third (C3) 760 m inclined core, two microgranite sheets were intersected, and a total of 6.7 m of the core was mapped as microgranite. No orientation data were collected for the sheets in the cores implying that sheet thicknesses are not corrected for intersection bias. All drill holes intersected intermittent subvertical to subhorizontal brecciated and heavily altered zones. A prominent approximately 10 m wide subvertical alteration and deformation zone (corrected for drill hole inclination) was noted in Core 3 about 500 m North of C3 in Figure 2 at a depth of approximately 400 m. The altered part of the core coincides with a topographical trough (Figures 1b and 2).

3. Methods

In total 54, oriented block samples were collected from across the Götemar pluton in 2020 and 2021 for anisotropy of magnetic susceptibility analysis. The sample distribution targeted the coarse granite, medium-grained granite, and microgranite sheets to evaluate the strain record in a granitic magma mush. One oriented sample (GM-27) was collected from the granodioritic host rock to the pluton. Between six and 27 (avg. 15 per sample), 25 mm × 22 mm core (sub)specimens were extracted from each of the oriented block samples for rock magnetic

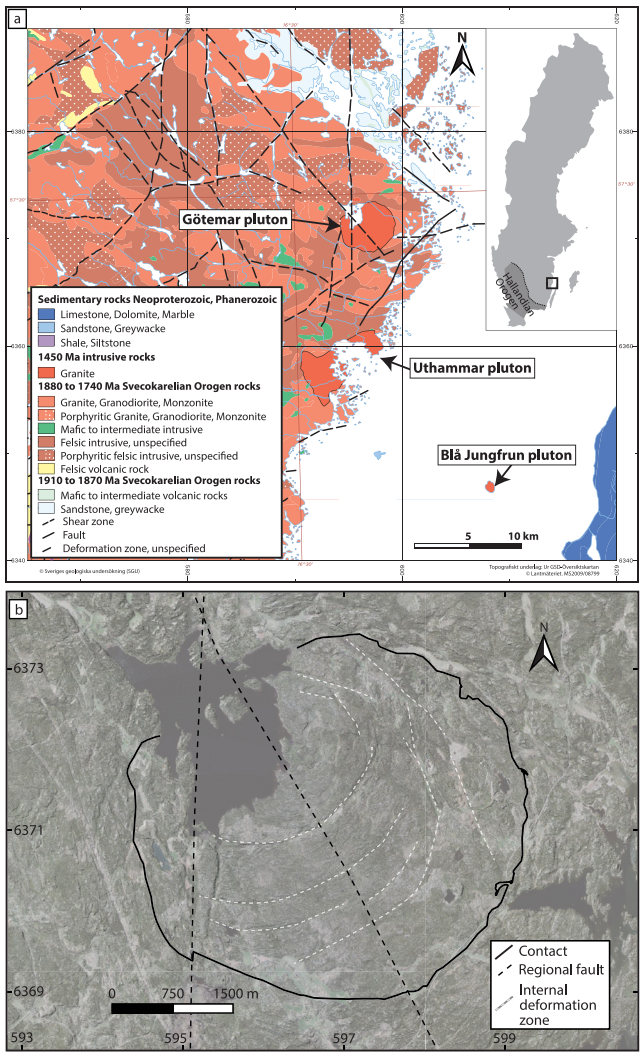

Figure 1. (a) 1:250000 scale geological map of the Götemar pluton and its surroundings. Note the nearby Mesoproterozoic Uthammar and Blå Jungfrun plutons. Modified from the Swedish Geological Survey map ©Sveriges Geologiska Undersökning (SGU, 2021). The location of the Hallandian Orogen is shaded on the inset map of Sweden based on data in Ulmius et al. (2015). (b) Satellite image draped over a digital elevation model of the Götemar pluton and the surrounding area (Orthophoto RGB 0.25 m ©Lantmäteriet 2021, höjddata grid 2+ ©Lantmäteriet 2021, License: Forskning, utbildning och kulturverksamhet). Regional faults with documented vertical displacement are indicated on the map. Along the westernmost fault, displacement has been estimated to be 500 m (Kresten & Chyssler, 1976). Coordinate system: UTM 33N, WGS 84.

analysis undertaken at the M^{3}Ore lab at the University of St. Andrews. The shape of the exposure of granite sheets wider than 1 m was traced with a hand-held Dual frequency GPS, and contact orientations were measured with the FieldMove Clino app using an iPhone. The inclination and orientation of microgranite and pegmatite sheets <1 m wide were measured using the FieldMove Clino app.

3.1. Anisotropy of Magnetic Susceptibility

Low-field in-phase AMS was measured on each sub-specimen with a KLY-5 Kappabridge using a 3D automatic spinning holder in a field of 400 A/m and with a frequency of 1440 Hz. Sub-specimen data were used to calculate a mean symmetric second-rank magnetic susceptibility tensor using the least square inversion method of Jelínek (1978). The magnetic susceptibility tensor defines the length and orientation of the three orthogonal principal axes of susceptibility $k_1 \geq k_2 \geq k_3$ (Khan, 1962). Fabric parameters used to describe the magnetic fabric are summarized in Tarling and Hrouda (1993). The mean magnetic susceptibility (Km) is given by

$$K_m = \frac{k_1 + k_2 + k_3}{3}$$

The corrected degree of anisotropy is given by the anisotropy parameter P_j, and the shape of the anisotropy is given by the T parameter, as originally defined by Jelínek (1981), and calculated using the software *Anisoft5* (Chadima et al., 2019). The corrected degree of anisotropy is defined as

$$P_j = \exp\sqrt{2\left((\eta_1 - \eta_m)^2 + (\eta_2 - \eta_m)^2 + (\eta_3 - \eta_m)^2\right)}$$

where $\eta_x = \ln(k_x), x = 1,2,3$ and $\eta_m = \frac{\eta_1+\eta_2+\eta_3}{3}$. The shape ($T$) parameter is given by

$$T = \frac{2\eta_2 - \eta_1 - \eta_3}{\eta_1 - \eta_3}$$

The magnetic susceptibility ellipsoid shape can range from rotational oblate ($T = 1$) to rotational prolate ($T = -1$) or present a triaxial neutral fabric ($T \approx 0$). A P_j value larger than 1 defines an anisotropic fabric.

3.2. Anisotropy of Anhysteretic Remanence Magnetization

The anisotropy of anhysteretic remanence magnetization (AARM) was measured on seven to 12 sub-specimens from selected samples (see section below) to identify carriers of AMS and reveal magnetically inverse fabrics or magnetic sub-fabrics (Ferré, 2002). The following AARM analytical procedure was used; (a) Sub-specimens were individually demagnetized with an Agico LDA5 using a 2-axis tumbler and a peak alternating demagnetization field (AF) of 200 mT, (b) an ARM was imparted along a single axis of each sub-specimen using a peak AF of 180 mT and DC field of 500 μT using a PAM1 Agico magnetizer, (c) the magnetization acquired by the sub-specimen was measured in an Agico JR6-a Magnetometer, (d) steps 1 to 4 were repeated in 6-positions following the B-mode measurement scheme (Hext, 1963; Jelínek, 1977). ARM field strengths were determined based on ARM acquisition and demagnetization experiments (Figure S2 in Supporting Information S1). The AARM data were processed and the principal axes of remanence ($R_1 \geq R_2 \geq R_3$) were calculated using a mean symmetric second-rank tensor and reoriented to a geographical coordinate system in the REMA6 software (Chadima et al., 2018).

10.1029/2023GC011061

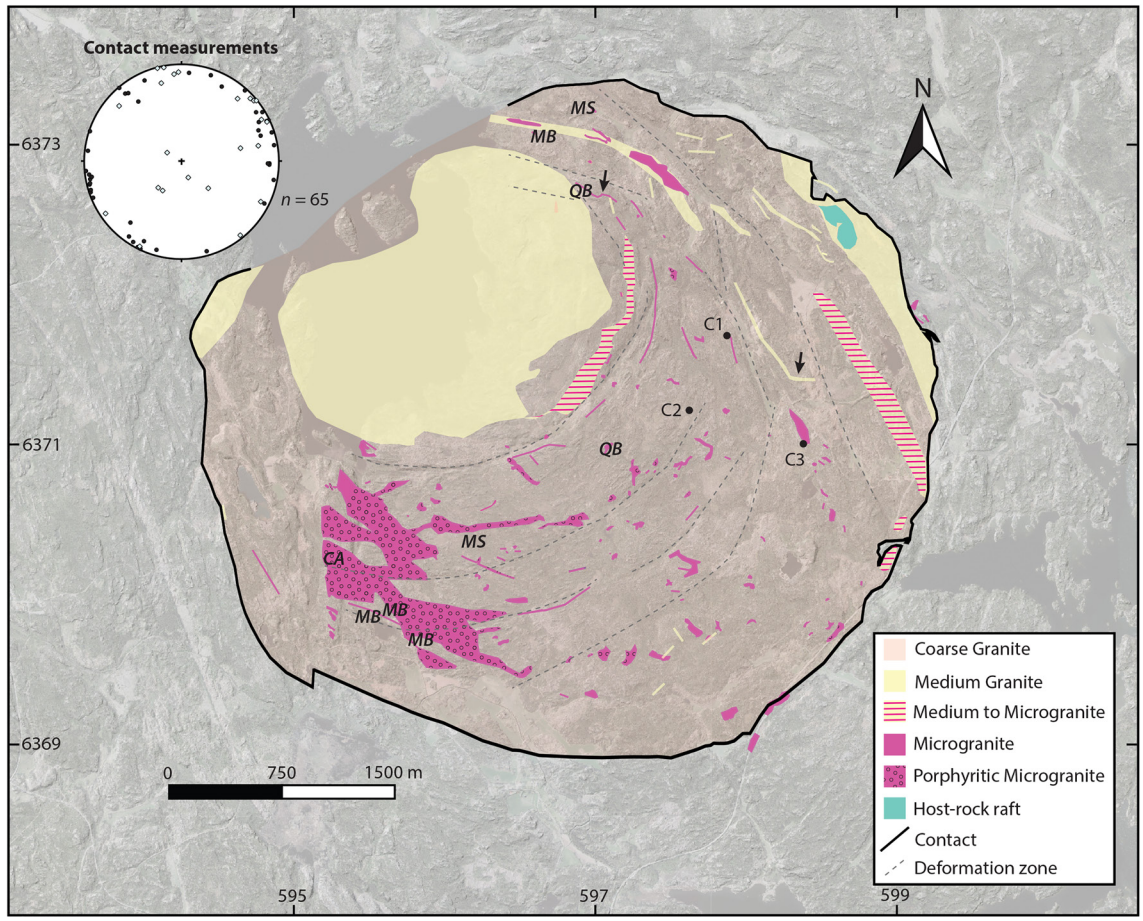

Figure 2. Mapped medium-grained granite and microgranite sheets overlaid on a satellite image of the Götemar pluton. The core locations of Scherman (1978) are marked on the map. The black arrows mark sharp bends in sheet exposures that indicate a change from a vertical to a horizontal sheet attitude along the sheet strike. Host-rock contact measurements are displayed as poles in the equal-area lower hemisphere stereonet and show an essentially vertical contact (coarse-grained granite, black circles, and microgranite and medium-grained granite, hollow diamonds). The locations for observations of quartz bands (QB), mafic banding (MB), and crystal alignment (CA) in microgranite sheets and biotite (mafic) segregations (MS) in coarse-grained granite are indicated on the map. Coordinate system: UTM 33N, WGS 84. See Figure S1 in Supporting Information S1 for raw GPS data collected during this study used to create the geological map. All structural measurements and sheet GPS data are provided by Mattsson et al. (2023).

3.3. Characterization of Magnetic Carriers

To identify the magnetic carriers in the sub-specimens, we performed several magnetic characterization experiments. Representative high (*Km* between 1.3×10^{-2} and 2.7×10^{-3} SI; GM-16, GM-19, GM-25, GM-28 and GM-31) and low mean susceptibility sub-specimens (*Km* between 3.0×10^{-4} and 3.4×10^{-5} SI; GM-01, GM-03, GM-04, GM-10, GM-20 and GM-22) were selected for the characterization experiments. Samples GM-04, GM-10, and GM-20 represent microgranite and medium-grained granite, whereas all other selected sub-specimens are from coarse-grained granite.

The temperature dependence of the bulk magnetic susceptibility of each sample was determined using a KLY-5 Kappabridge and CS-4 attachment. Each sample was pulped with a ceramic pestle and mortar, and a ~0.35 g pulp sample was cooled to −194°C using liquid Nitrogen in an Agico CSL cryostat; the bulk magnetic susceptibility of the sample was then measured as the sample heated up to 0°C. The pulp sample was subsequently saturated in an Argon atmosphere in an Agico CS4 furnace and the bulk magnetic susceptibility was measured as the sample was heated from 20°C to 700°C and cooled back to room temperature at a rate of 12°C/min. The pulped sample was then cooled to −194°C and bulk magnetic susceptibility was measured until the sample temperature reached 0°C.

Magnetic coercivity and temperature unblocking experiments were also carried out on the selected sub-specimen set with a view to identifying the coercivity properties of each sub-specimen and aiding the interpretation of

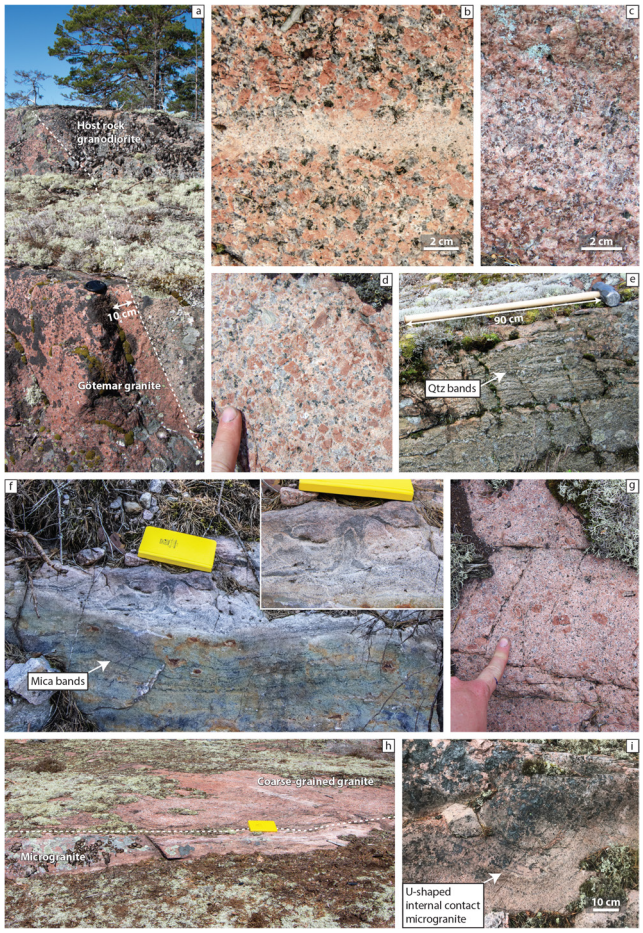

Figure 3. (a) Sharp contact between a granodioritic host-rock raft and the Götemar granite in the northeastern part of the pluton (see Figure 2 for location). The contact is traced by the white dashed line. Lens cap for scale. (b) Coarse-grained granite intruded by a microgranite dike. (c) Close-up of pale medium-grained granite. (d) Coarse-grained granite with microgranite groundmass displaying the gradational contact relationship that exists between some microgranite sheets and the coarse-grained granite. (e) Subhorizontal sheet of microgranite with bands of large quartz crystals. (f) Subhorizontal mica banding in a microgranite sheet. Inset of a diapiric melt protrusion disturbing the compositional banding. (g) Close-up of porphyritic microgranite. (h) Subhorizontal contact between coarse-grained granite and a microgranite sheet. The contact is highlighted by the white dashed line. Note the discordant light microgranite sheet protruding from the subhorizontal sheet in the upper right-hand side of the image. (i) U-shaped internal contact in a microgranite sheet.

the AMS data. These experiments included acquisition and demagnetization of Anhysteretic Remanent Magnetization (ARM) and Isothermal Remanent Magnetization (IRM, up to 3 T), demagnetization of Natural Remanence Magnetization (NRM), and backfield IRM experiments based on Lowrie and Fuller (1971) and Dunlop and Özdemir (1997). All experiments were completed using a JR6-a magnetometer, LDA5 AF demagnetizer, PAM1 magnetizer, and a MMPM 10 pulse magnetizer. A modified three-component demagnetization experiment based on Lowrie (1990) was the last experiment performed on the sub-specimens. Three-component demagnetization is used to measure the relative contribution made by magnetic remanence carrying grains to a sample's bulk magnetic remanence modulus based on the user-selected coercivity values and unblocking temperature. IRMs of different strengths were imparted along the $Z+$ (3 T), $Y+$ (0.3 T), and $X+$ (0.03 T) axes of the specimens using the MMPM 10 pulse magnetizer. The samples were then thermally demagnetized with an MMTD demagnetizer from Magnetic Instruments in steps of 50 to 20°C from 100 to 700°C using a temperature linger time of 25 min. The bulk magnetic susceptibility of the sub-specimens was measured with the KLY-5 between each demagnetization step to identify alteration during heating. Expanded analytical details of the magnetic characterization experiments are given in the associated data publication (Mattsson et al., 2023).

4. Results

4.1. Field Relationships

Visible exposures of the contact between the Götemar granite and its host rock are sharp and dominantly steeply dipping (Figures 2 and 3a). The granodioritic host rock close to the northeastern and eastern contact of the pluton is intruded by a few subhorizontal medium-grained granite and microgranite sheets of Götemar granite (Figure 2). A host/wall rock raft is observed enveloped by the Götemar granite in the northeastern part of the pluton. The observed contacts between the coarse-grained and medium-grained granite are sharp. In addition to the large body of medium-grained granite in the northern part of the pluton, several contact-parallel medium-grained granite sheets occur in the eastern and northeastern parts of the pluton (Figure 2). Vertical medium-grained granite sheets have observed thicknesses of up to 5 m. The thicknesses of subhorizontal medium-grained granite sheets, on the other hand, are difficult to determine but are assumed to range from a couple of meters to tens of meters as inferred by the borehole data of Scherman (1978). Exposure widths of subhorizontal sheets in the northeastern part of the pluton are sometimes >100 m. Contact parallel (arcuate) sheets of microgranite occur throughout the pluton (Figure 2). The microgranitic sheets within the pluton are both porphyritic and aphyric (equigranular), and sometimes range from medium-grained granite to microgranite textured (Figures 2 and 3g). The contacts between the microgranite sheets and the coarse-grained granite vary from sharp, undulating, lobate to gradational (Figures 3d and 3h). Many sheets are internally heterogeneous in terms of the number of phenocrysts. Subvertical exposures of contacts between the phenocryst-rich and phenocryst-poor parts of sheets are U-shaped (Figure 3i). The thickness of individual microgranite sheets ranges from a couple of centimeters up to tens of meters and their attitudes range from horizontal or gently inclined to subvertical (Figure 4). A change in the sheet attitude along strike from subvertical to subhorizontal can be observed at two localities; this is shown on the map as relatively sharp bends in the sheet strike (Figure 2). In the northeastern part of the pluton, the apparent thickness of sheet exposures becomes wider along strike toward the South as the dips of the sheet changes from subvertical to subhorizontal (Figure 2). Subhorizontal quartz or mica compositional bands that are parallel to the sheet contacts are observed at the margins of some thicker microgranite sheets

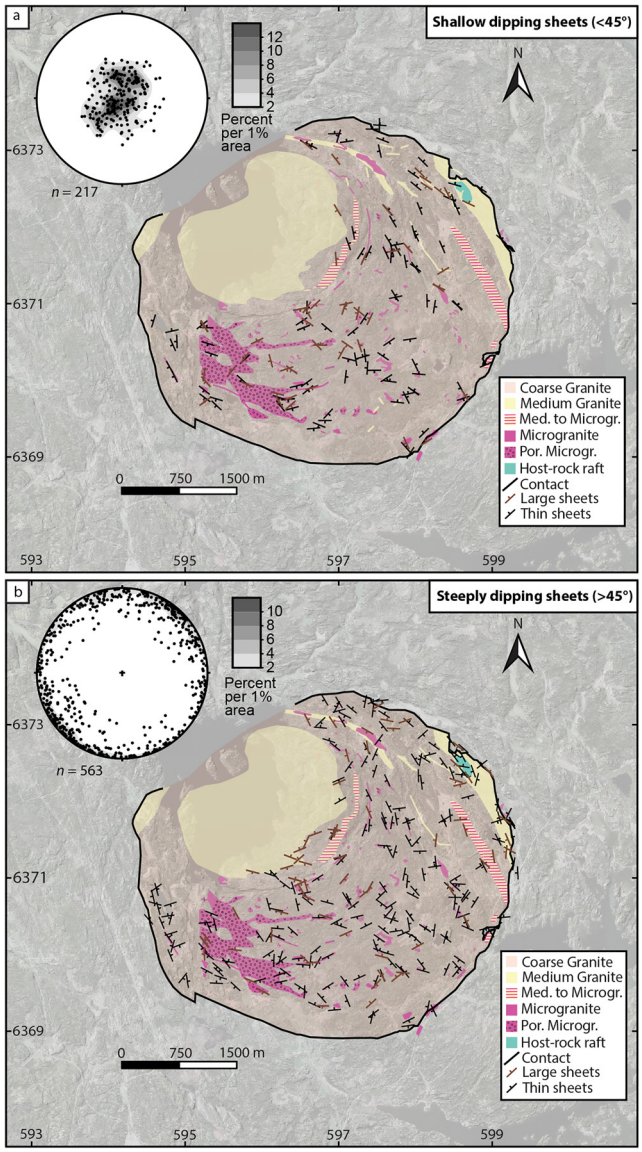

Figure 4. (a) Shallow (<45°) and (b) steeply dipping sheets (>45°). Both thin sheets (<1 m wide) and large granite sheets (>1 m wide) are displayed on the map. Some sheet measurements are not shown to limit cluttering. Poles to the sheet planes are plotted in equal-area lower hemisphere stereonets. The stereonets were created with the software Stereonet 11 (Allmendinger et al., 2012). Coordinate system: UTM 33N, WGS 84. All measurement data are provided in the associated data set (Mattsson et al., 2023).

(Figures 2 and 3e, f). Within equigranular fine-grained microgranite sheets, pegmatitic alkali feldspar megacrysts occasionally occur at the sheet margin. Weak alkali feldspar phenocryst alignment is observed in one of the major sheets in the southwestern part of the pluton (Figure 3g). No distinct mineral alignment has been observed elsewhere in the Götemar pluton.

Four sets of thin microgranite sheets (<1 m wide) are identified based on their orientation relative to the pluton's contacts, (a) shallow to moderately dipping sheets that dip away from the main body of medium-grained granite, and (b) steeply dipping sheets that strike parallel to the concentric deformation zones within the pluton (see Figure 1b), (c) steeply dipping NW-SE striking sheets and (d) ENE-WSW striking steeply dipping sheets (Figure 4b). Larger microgranite sheet contacts are not always well exposed; however, where orientation measurements are possible, steeply and shallow dipping contacts are observed (Figure 4a). In several locations, the thin sheets are separated into parallel anastomosing branches that are up to 1 m wide. Angular-shaped exposures of microgranite have been observed at two localities within the coarse-grained granite, which could indicate the stoping of coarse-grained granite into intruding microgranite magma sheets.

4.2. Magnetic Carrier Characterization

Temperature versus susceptibility (T-χ) specimen data depict definite trends that help characterize their magnetic mineralogy. Samples with a relatively high magnetic susceptibility (Km between 1.3×10^{-2} and 2.7×10^{-3}; GM-16, GM-19, GM-25, GM-28, and GM-31) show a distinct Verwey transition at −160°C before and after the heating cycle (Figure S2 in Supporting Information S1). These features indicate the dominance of near stoichiometric magnetite (Dunlop & Özdemir, 1997). During heating the samples' susceptibility increases from 450°C to about 550–570°C when a large drop in susceptibility is recorded, which shows that low-Ti magnetite is the main carrier of the magnetic susceptibility (Akimoto, 1962; Lattard et al., 2006).

Samples with low susceptibility (Km between 3.0×10^{-4} and 3.4×10^{-5}; GM-01, GM-03, GM-04, GM-10, GM-20, and GM-22) show a fairly flat susceptibility curve up to 400°C after which the susceptibility increases before dropping again between 550 and 600°C (Figure S2 in Supporting Information S1). All low-susceptibility specimens display increases of >50% in susceptibility between heating and cooling, which points to the destruction of low-susceptibility phases such as maghemite or Ti-maghemite and the growth of a high-susceptibility phase during the measurement (Dunlop & Özdemir, 1997). The occurrence of a prominent ~580°C Curie temperature after heating to 700°C and an enhanced Verwey transition during step 3 is consistent with the growth of near stoichiometric magnetite during the heating cycle (Dunlop & Özdemir, 1997; Özdemir et al., 1993).

4.2.1. IRM Acquisition

IRM acquisition profiles identify three general groups: (a) Specimens that are not fully saturated in a field of 3 T (GM-01, 03, 10, 20, and 22), which we call high coercivity samples. (b) Specimens that reach 90% saturation in fields between 0.16 and 0.5 T (GM-16, 19, 28, and 31), which we call low coercivity samples. (c) Specimens with an intermediate coercivity between group (a) and (b) (GM-04 and 25) (Figure 5a and Figure S2 in Supporting Information S1). The specimens with the highest coercivity have the lowest mean magnetic susceptibility and vice versa.

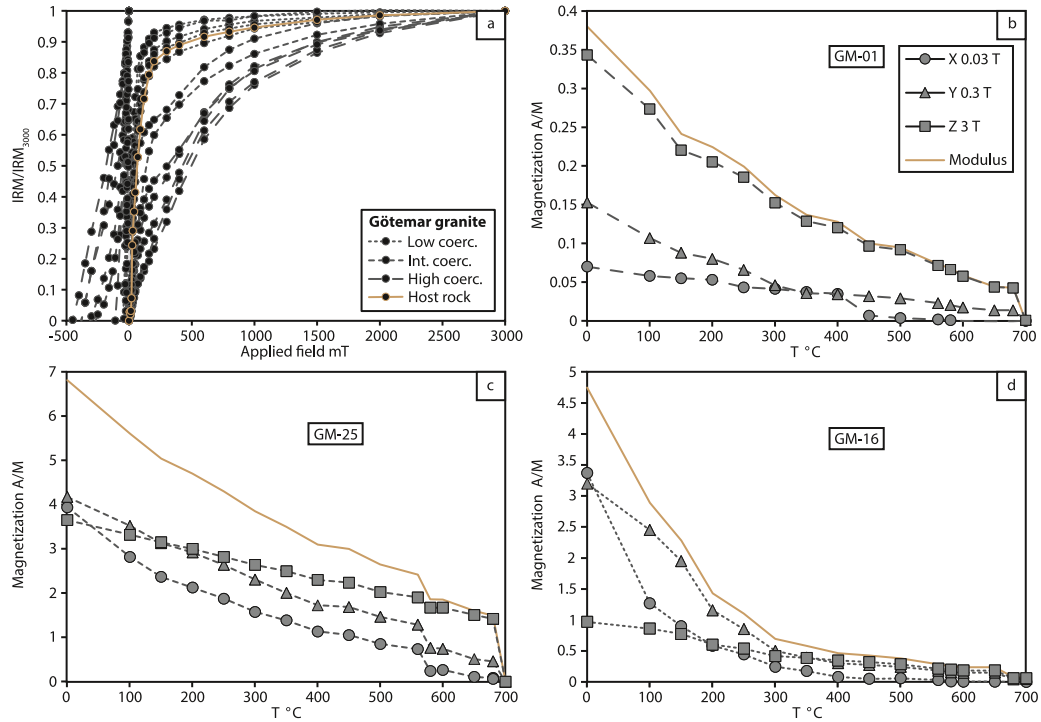

Figure 5. (a) IRM acquisition and BIRM imparted along the *Z*+ and *Z*− axes of the selected specimens, respectively. Examples of three-component demagnetization of sub-specimens with (b) high-, (c) intermediate- and (d) low-coercivity according to the IRM acquisition (a). Magnetization strength is given in ampere per meter (A/M). All magnetic characterization data are plotted in Figure S2 in Supporting Information S1.

4.2.2. ARM and IRM Demagnetization

The ARM AF demagnetization on the sub-specimens with high coercivity displays Median Destructive Fields (MDFs) when half of the imparted magnetization has been removed between an AF of 15–30 mT. Low coercivity samples reach the MDF with an AF below 10 mT (Figure S2 in Supporting Information S1). Sub-specimens with intermediate coercivity (GM-04 and GM-25) display ARM MDFs of approximately 25 and 8 mT, respectively. Most samples reach $M_{ARM}/M_{max} = 0.1$ at fields above 100 mT.

The AF demagnetization of the imparted IRM in most of the high coercivity sub-specimens approaches the MDF at an AF of 200 mT. GM-22, which belongs to the high coercivity group of samples, records an MDF of approximately 150 mT. The low coercivity samples reach the MDF at an AF between 5 and 15 mT. Intermediate coercivity sub-specimens GM-04 and GM-25 reach the MDF at around 70 and 20 mT, respectively (Figure S2 in Supporting Information S1). All sub-specimen retained at least 10% of the imparted magnetization ($M/M_{IRM3000} = 0.1$) at a field of 200 mT.

4.2.3. Three Component Demagnetization

All results of the modified three-component demagnetization experiment after Lowrie (1990) are presented in Figures 5b–5d and Figure S2 in Supporting Information S1. Magnetic remanence in all high coercivity specimens (i.e., GM-01, 03, 10, 20, and 22) is dominated by the 3 T *Z*-axis and shows that approximately 40%–70% of the magnetic remanence is controlled by minerals that saturate in fields above 3 T. The 3 T *Z*-axis from these samples also displays nearly linear demagnetization with about 80% of the imparted remanence magnetization removed between 20°C and ~650°C with an abrupt decrease between ~650°C and 700°, resulting in 95%–100% removal of the imparted magnetization. This profile is consistent with the presence of hematite (Lowrie, 1990) (Figure 5). The 0.03 T *X*-axis demagnetization data from the same high coercivity specimens demagnetize nearly linearly until 580°C when the imparted field is completely removed, indicating the presence of low coercivity magnetite in these samples (Figure 5b; Figure S2 in Supporting Information S1).

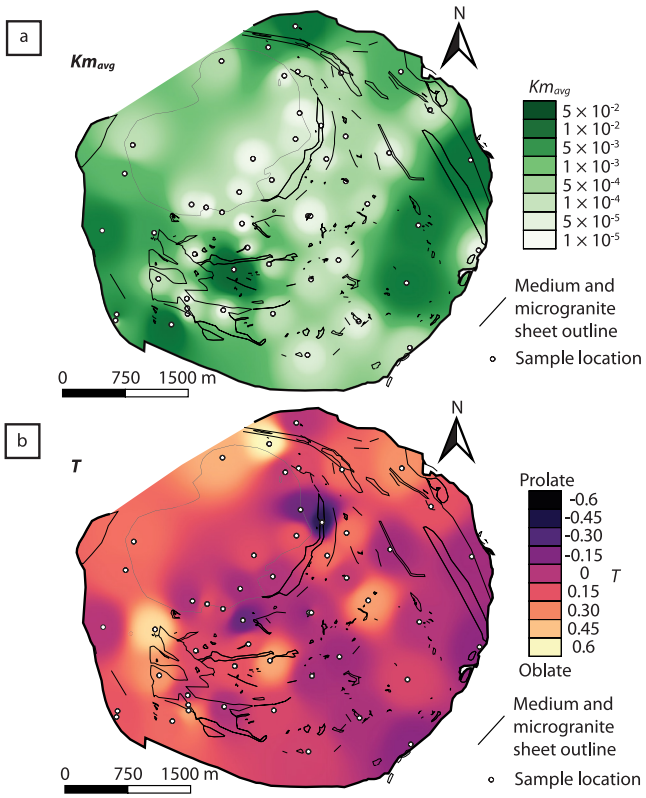

Figure 6. Contour maps of AMS fabric parameters calculated using Inverse-Distance Weighting. The outlines of medium-grained granite and microgranite sheets are shown on the map. (a) Sample average mean magnetic susceptibility, *Km*. (b) Sample average shape factor, *T*. Note that the contour scale has been bracketed between 0.6 and −0.6 to better highlight differences in the AMS fabric shape.

In contrast, magnetic remanence in all low coercivity specimens (i.e., GM-16, 19, 28, and 31) is dominated by the 0.03 T *X*-axis, with approximately 40%–60% of the magnetic remanence being controlled by minerals that saturate in fields below 0.03 T. The data also show that a substantial contribution (~20–40%) is also derived from the 0.3 T *Y*-axis and that the 3 T *Z*-axis generally contributes >20% of the remanent magnetization. About half of the IRM imparted along the *X*-axis (0.03 T) and *Y*-axis (0.3 T) is lost in the first heating step, and the magnetization later decreases until 450°C when the bulk of the imparted IRM is gone. This indicates that low coercivity grains such as multi-domain magnetite dominate the *X*-axis 0.03 T contribution. The 3 T *Z*-axis hard component in the low coercivity specimens shows a steady decrease in magnetization until the imparted magnetization is removed at around 680°C, signifying the occurrence of relatively small amounts of maghemite and/or hematite (Figure 5d).

The intermediate coercivity specimen GM-25 shows linear decay of all components until 580°C, where the magnetization drops to ~10% of the initial magnetization (Figure 5c). The magnetization is subsequently completely removed at 700°C, indicating that both magnetite and hematite are present in the sample. In GM-04, the magnetization of all components drops slightly at 580°C and is removed between 650 and 680°C; this is also consistent with the presence of magnetite and Ti-maghemite, respectively. The presence of maghemite in the samples is revealed by rapid decay of the magnetization of the intermediate component (*Z*-axis) until 300–350°C and loss of magnetization between 600 and 650°C (Dunlop & Özdemir, 1997; Lowrie, 1990). Additionally, maghemite is indicated by the bump in the T-χ heating curve in GM-04, 19, 22, and 31 between 250 and 350°C (Figure S2 in Supporting Information S1) (Bilardello, 2020; Dunlop & Özdemir, 1997; Petronis et al., 2011).

Changes in the specimens' bulk magnetic susceptibility during thermal demagnetization show that alteration occurred during the 3-component experiment (Figure S2 in Supporting Information S1). Large changes in bulk susceptibility are recorded in all specimens between 300 and 500°C (Figure S2 in Supporting Information S1) and could be caused by the alteration of (Ti-)maghemite to hematite, which usually occurs between 250 and 400°C (Bilardello, 2020; Dunlop & Özdemir, 1997; Tauxe et al., 2018). An increase in magnetic susceptibility during heating as observed in GM-04 may be linked to the formation of magnetite (Figure S2 in Supporting Information S1) (Liu et al., 2005; Petronis et al., 2011). The three-component demagnetization experiments reveal a magnetic mineralogy consisting of magnetite, maghemite, and hematite in most of the specimens, but with different relative abundances.

4.3. Magnetic Fabrics

The orientation of the mean AMS principal axes records a broad range of orientations between sample sites (Figures S3a and S3b in Supporting Information S1). The samples' mean susceptibility (*Km*) ranges from 1.04×10^{-5} to 2.72×10^{-2} SI with an average of 2.78×10^{-3} (1σ, 5.72×10^{-3}, $n = 54$) (Figure 6a). The average corrected degree of anisotropy (*Pj*) of all the analyzed samples is 1.06 (1σ, 0.04) ($n = 54$). The coarse-grained granite samples have an average *Km* of 4.61×10^{-3} SI (1σ, 6.96×10^{-3}, $n = 30$) and an average P_j of 1.08 (1σ, 0.03). The average *Km* of the medium-grained granite samples is 7.68×10^{-5} SI (1σ, 7.19×10^{-5}, $n = 12$) with an average P_j of 1.04 (1σ, 0.01). The microgranite samples have an average *Km* of 5.68×10^{-5} SI (1σ, 3.81×10^{-5}, $n = 10$) and an average P_j of 1.04 (1σ, 0.02). The highest *Km* values can be found close to the eastern, western and northern contact to the pluton and in areas rich in mafic mineral segregations, whereas the center of the Götemar pluton has relatively low *Km* (Figure 6a). The fabric shape parameter *T* in coarse- and medium-grained granite and microgranite vary between sub-specimens and consequently results in an averaged triaxial fabric in most samples (Figure 6b). However, the AMS fabric shape in the western and northern marginal zones is dominantly oblate

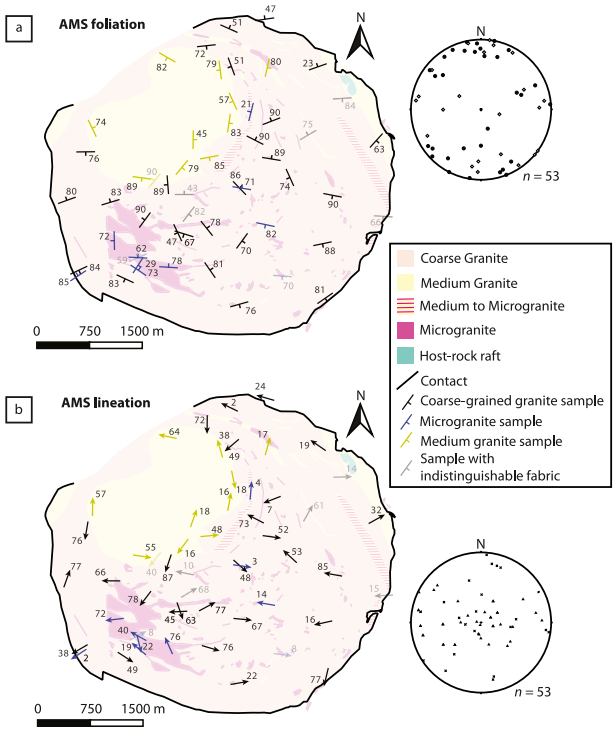

Figure 7. Mean in-phase AMS foliations (a) and lineations (b) of the Götemar granite samples. Samples with a large dispersion of sub-specimen principal axes (i.e., indistinguishable fabric) are semi-transparent. The poles to the AMS foliations and the AMS lineations (k_1) are plotted in the inset equal-area lower hemisphere stereonets. Foliation poles for coarse-grained granite are given as black circles and medium-grained granite and microgranite sheet foliation poles are plotted as hollow diamonds. Lineations for coarse-grained granite are given as black triangles and medium-grained granite and microgranite sheet lineations are plotted as crosses. Sub-specimen principal axes of susceptibility are shown in stereonets in Figures S3a and S3b in Supporting Information S1.

both in coarse-grained and medium-grained granite units, whereas the fabric is triaxial to prolate in the central and eastern parts of the pluton. A dominantly prolate to transitional prolate fabric is recorded in samples collected in proximity to the northeastern contact of the main medium-grained granite body (Figure 6b). Individual sub-specimen axes delineate well-defined 95% confidence ellipses in the majority of the samples indicating that whereas the orientation of individual sub-specimen principal axes varies, the fabric detected at sample scale is reliable (Figure S3 in Supporting Information S1).

The AMS foliations and lineations of the medium-grained and microgranite sheets strike and trend largely parallel to both the internal granite-granite contacts and the granite-host rock contact (Figure 7). In the coarse-grained granite, both host rock-granite contact parallel and perpendicular AMS foliations occur. Oblique (i.e., not contact parallel) AMS foliations in the center of the pluton are steeply dipping and strike NNW-SSE, whereas oblique AMS foliations close to the margins of the pluton strike ENE-WSW. AMS lineations in the coarse-grained granite are either moderate to shallowly plunging and contact parallel, or steep to moderately plunging and trending highly oblique to the concentric pluton structure (Figure 7b).

4.3.1. AARM

Nine samples were selected for AARM analysis (Figure S4 in Supporting Information S1). The AARM fabric of GM-01 and GM-03 were not analyzed due to the disperse orientations of the AMS principal axes (see Figure S3 in Supporting Information S1). The K_{rem} (mean remanence) of the samples ranges from 8.5×10^{-5} to 2×10^{-3}. The average corrected degree of anisotropy (P_j) of the analyzed sample set is 1.15 (1σ, 0.07). The average AARM shape factor T of all analyzed samples ranges from 0.24 to −0.18, representing transitional to triaxial fabric shapes.

5. Discussion

5.1. Deciphering the AMS Fabric in the Götemar Pluton

AMS in igneous rocks is often controlled by the shape and/or distribution of ferrimagnetic grains owing to their susceptibility values which are an order of magnitudes higher than silicate paramagnetic phases such as micas, pyroxenes, and amphiboles (Biedermann, 2018; Borradaile & Jackson, 2010; Gaillot et al., 2006; Grégoire et al., 1998; Hargraves et al., 1991; Mattsson et al., 2021; Rochette et al., 1999; Stephenson, 1994). The magnetic mineralogy of a sample greatly impacts the relationship between the shape and orientation of the AMS tensor and the true petrographic rock fabric (Borradaile & Jackson, 2010; Tarling & Hrouda, 1993). Here, we evaluate our magnetic characterization data to validate our AMS data set.

A correlation between the corrected degree of anisotropy (P_j) values and mean susceptibility (Km) values is generally observed within the Götemar pluton (Figure S5 in Supporting Information S1). Such a relationship is a common feature in rocks with AMS P_j values < 1.15 whose mean susceptibility is controlled by the relative abundance of ferrimagnetic minerals, such as magnetite (Borradaile & Jackson, 2010; Hrouda, 1982; Tarling & Hrouda, 1993). Rock magnetic data from GM-16, 19, 28, and 31 represent coarse-grained granite and consistently show that low coercivity magnetite (likely multi-domain), best illustrated by a magnetically saturated IRM acquisition curve and a Curie temperature of ~580°C, is the dominant magnetic mineral in these samples (Figure S2 in Supporting Information S1; Figure 5a). The high coercivity specimens GM-01, 03, 10, 20, and 22 (representing all the rock units of the pluton) have a markedly different magnetic mineralogy that is characterized by concave IRM acquisition curves, higher MDFs of IRM and ARM demagnetization and very low mean susceptibility values in the order of $\sim 1 \times 10^{-4}$ SI (Figure S2 in Supporting Information S1; Figure 5a). These results point toward the dominance of higher coercivity mineral phases such as Ti-maghemite. Data arising from T-χ experiments on high coercivity samples show irreversible heating-cooling curves and indicate that magnetite grew during

the experiment, possibly at the expense of Iron-sulfide minerals, such as pyrite, that were oxidized and replaced by magnetite. Three-component demagnetization results concur with these observations and suggest that low coercivity magnetite, represented by the 0.03 T *X*-axis, is present in small quantities in analyzed sub-specimens, while magnetic remanence is dominantly carried by high coercivity phases such as hematite (Figure 5b). The very low *Km* values observed in GM-01, 03, 10, 20, and 22 indicate that ferrimagnetic minerals constitute only a small proportion of these sub-specimens and it is therefore possible that paramagnetic minerals control the AMS signal. A comparison between AARM and AMS results efficiently tests this possibility because AARM should reflect the fabric of low coercivity magnetic grains (most likely magnetite) and hence elucidate the relationship between AMS and the magnetite shape or distribution fabric in our sample set (Borradaile & Jackson, 2010; Jackson, 1991; McCabe et al., 1985).

The AARM principal axes (R_x) are coaxial to the AMS principal axes (k_x) in GM-04, GM-22, and GM-25 (Figure S4 in Supporting Information S1). In GM-31, R_1 axes are steeply plunging but with disperse trends, and R_2 and R_3 axes are plotting on a subhorizontal girdle. However, the mean principal AARM axes of GM-31 plot close to the AMS principal axes. The AARM of some of the samples reveals magnetically intermediate magnetic fabrics where $k_1 = R_2$ or $k_3 = R_2$ (cf. Ferré, 2002). For example, in GM-19 AARM R_2 and AMS k_3 axes plot close to each other (Figure S4 in Supporting Information S1). However, magnetically inverse AMS ($k_1 = R_3$) have not been observed in the selected samples. GM-10, GM-16, GM-20, and GM-28 show dispersed R_1 orientations and display AARM foliations that are slightly oblique relative to the AMS foliations, which point to the presence of a magnetic sub-fabric that affects the remnant magnetization tensor. The intermediate AMS-AARM (e.g., $k_1 = R_2$) fabric relationship seen in some of the coarse-grained granite samples indicates that the AMS foliations are a more reliable indicator for the petrofabric in the coarse-grained granite than the magnetic lineations (k_1). Low mean susceptibility medium-grained granite samples (GM-04 and 20) have a coaxial and magnetically intermediate AMS-AARM relationship, which infers that the AMS fabric of these samples most likely reflects the petrofabric of low coercivity remanence carrying grains and not paramagnetic minerals.

The cause of the large spatial differences in mean susceptibility (*Km*) within the Götemar pluton could be related to the hydrothermal to metasomatic alteration previously noted in and around the pluton (Figure 6a) (Drake et al., 2009; Friese et al., 2012; Tillberg et al., 2019). The low mean susceptibility may therefore correspond to areas with a magnetic fabric created by secondary alteration processes. However, the comparatively low mean susceptibility values of medium-grained granite and microgranite could also indicate that the primary magma composition of those units was relatively magnetite-poor compared to the coarse-grained granite magma. This notion is supported by the medium-grained granite AMS foliations and lineations, which correlate with the unit contact orientation, and therefore suggest a primary origin of the magnetic fabric related to magma emplacement (Figure 7).

5.2. Emplacement of Magmatic Sheets in the Götemar Pluton

This section summarizes and discusses the structures and magma transport features of the Götemar pluton. The concentric internal structure of the Götemar pluton is emphasized by the curved contact-parallel topographical troughs seen in satellite images of the pluton (Figure 1b). One of these curved features can be correlated with a 10 m wide brecciated and altered zone in Core 3 (Scherman, 1978). The saw-tooth shape of the eastern contact with the major microgranite sheet (in the southwestern part of the pluton) coincides with the topographical troughs, which suggests that these features are associated with displacement and can be classified as shear zones or faults (Figure 2). However, the sense of displacement and state of deformation (brittle or ductile) across these structures are difficult to determine due to the vegetation cover in the area; therefore, we prefer the generic term deformation zone to describe the features. Large medium-grained granite and microgranite sheets that dominantly strike parallel to the pluton-host rock contact and the internal deformation zones occur throughout the pluton (Figure 2). In the northern and southwestern parts of the pluton, sheet exposures are continuous for up to a kilometer along strike. A change from vertical to subhorizontal sheet attitude can also be observed by following sheets from the North toward the southeastern and central part of the pluton (Figure 2). In the central part of the pluton, sheets wider than 1 m are interpreted to be dominantly subhorizontally inclined with undulating contacts, since their exposures are not continuous along strike and some sheets display subhorizontal compositional banding (Figures 2 and 3e, f). We interpret that the feeder to the concentric sheets was located in the northwestern part of the pluton based on two main lines of evidence: (a) The position of the major medium-grained body in the

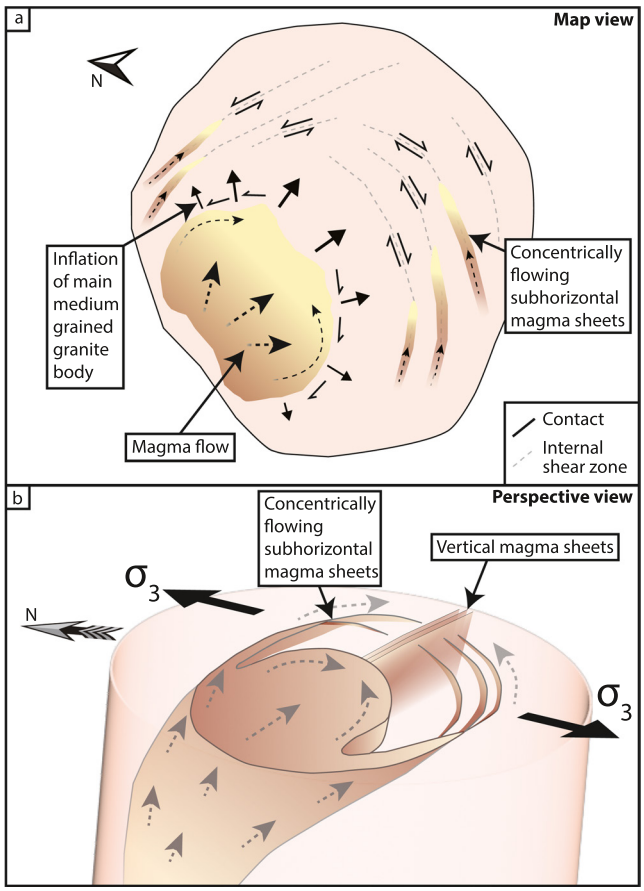

Figure 8. Conceptual model for the emplacement of medium-grained granite and microgranite sheets in the Götemar pluton. (a) Map view of the magma body, (b) perspective 3D view of the magma body. Magma was fed from the northwestern part of the magma body. To accommodate space for the magma intruding in the NW, the already emplaced highly viscous crystal mush was deflected vertically and laterally toward the East-southeast, facilitated by contact-parallel shear zones within the magma body. These shear zones were exploited by magma intruding into the magma mush, resulting in concentrically flowing subhorizontal sheets. Magma was also transported in vertical dikes dominantly striking NW-SE. The dike orientations are likely controlled by a back-arc extensional stress field related to the nearby Hallandian Orogen (see Figure 1a for location).

northwest and (b) that the microgranite sheets pinch out from the western and northern margin toward the southeastern part of the pluton, which indicates the magma propagation direction (Figures 2 and 8). The AMS fabric of the microgranite sheets supports the field observations of the sheet propagation direction and attitude. The AMS lineation indicates the stretching direction of the magma in sheets and has been shown to give a good approximation of the magma flow direction (e.g., Cañón-Tapia, 2004; Chadima et al., 2009; Geoffroy et al., 2002; Knight & Walker, 1988; Schmiedel et al., 2021). The AMS lineations in the Götemar microgranite sheet samples are shallow plunging and trending parallel to the sheet strike, except in the major microgranite sheet in the southwestern part of the pluton (Figure 7b). The lineations in the major microgranite sheet are moderately plunging and associated with sheet contact-parallel AMS foliations, which could indicate an overall up to the southeast migration of magma.

Quartz and mica bands occur in proximity to some sheet contacts in the southwestern and central parts of the Götemar pluton (Figures 3e and 3f). Compositional and textural banding features in silicic magma bodies could be related to crystallization fronts (e.g., comb layering and pegmatitic), mafic segregations (schlieren) or flow banding (Burchardt et al., 2019; Clemens et al., 2020; London, 2009; Mattsson et al., 2018; McCarthy & Müntener, 2016). Pegmatite crystallization fronts are associated with the formation of mafic banding in aplites (London, 2009). Pegmatite occurs within microgranite sheets in the Götemar pluton, but no pegmatites could be identified in close association with the mica bands, which is consistent with banding formation in a setting related to magma flow that inhibited the formation of pegmatite crystallization fronts. Mafic schlieren has been interpreted to form as flow segregations of mafic minerals in granitic magma accompanied by magmatic reactions (Clemens et al., 2020), whereas flow bands are compositional and/or textural differences in magma linked to flow partitioning, which promotes vesiculation and crystallization (Castro et al., 2005; Gonnermann & Manga, 2005; Tuffen et al., 2003). Since the Götemar granite magma was fluid-rich (Drake et al., 2009; Friese et al., 2012; Tillberg et al., 2019), volatile exsolution caused by strain-localization during magma flow could have promoted crystallization/segregation of quartz or mica in bands. Importantly, irrespective of how the banding formed, the existence of magma-derived banding shows that some of the Götemar microgranite sheets were melt-rich with limited crystal cargo (Figures 3e and 3f).

The AMS fabric shape distribution within the whole pluton shows a comparatively larger pure shear (oblate) component in the western and northern parts of the pluton, whereas the fabric is triaxial in the eastern and central parts (Figure 6b). The contact-parallel AMS foliations and lineations in the main medium-grained granite body largely reflect its shape and are consistent with the compaction of magma combined with subhorizontal contact parallel shear as the medium-grained granite body inflated and interacted with the coarse-grained magma mush (Figure 7). Notably, the sheets within the coarse-grained granite are dipping away from the main medium-grained granite body (Figure 4a). The dips of the subhorizontal sheets together with the contact-parallel medium-grained granite AMS fabric strongly suggest that the emplacement of the main medium-grained granite body deflected the coarse-grained crystal mush. The AMS foliations in the coarse-grained granite are contact-parallel in the northern and southern parts of the pluton (Figure 7a). However, in other areas of the pluton, the coarse-grained granite AMS foliations are oblique to the contact, either oriented NW to NNW-SE to SSE or ENE-WSW, parallel to the two groups of steeply-dipping sheets (c and d) in the pluton. The cause of the oblique fabrics in the center of the pluton is uncertain, but they could reflect the compaction of the mush as magma sheets intruded laterally into the mush and/or that the fabrics are secondary relating to post-emplacement alteration (see Figures 2, 6a, and 7). The contact-parallel deformation zones in the pluton supported by the triaxial AMS fabric in the central and

eastern parts of the pluton suggest that subhorizontal contact-parallel shear combined with some degrees of mush compaction accommodated the intrusion of magma into the granite magma body (Figures 1b, 6b, and 7). Considering that the host rock shows no evidence of deflection by the Götemar granite body (see Cruden, 2008), and the AMS fabric in the northern and western parts of the pluton are dominantly oblate, the prevailing expansion/growth direction of the magma body is assumed to be up accompanied by minor East-southeast lateral expansion.

5.3. Controls on Magma Transport Within Mushy Magma

It is widely established that large magma bodies are constructed in increments by pulses of magma (Bartley et al., 2006; Chan et al., 2017; Harry & Richey, 1963; Michel et al., 2008; Miller et al., 2018; Richey, 1928), and that within mid to upper-crustal granitic systems magma is transported in sheets (Hutton, 1988; McNulty et al., 1996; Miller & Paterson, 2001; Pignotta et al., 2010; Rocher et al., 2021; Weinberg & Searle, 1998). The Götemar pluton shows that magma sheet emplacement within mushy magma bodies is strongly influenced by the local magmatic and the regional stress field. The dominant NW-SE orientation of the steeply dipping thin sheets (>1 m wide) cannot be purely attributed to inflation-related stresses in the magma body (Figure 4b). These sheets (group c) are oriented parallel to the proposed orogenic front of the contemporaneous (1.47–1.38 Ga) nearby Hallandian Orogen (Figures 1a and 4b) (Bogdanova et al., 2014; Ulmius et al., 2015). Rocks deformed by the Hallandian Orogen are exposed South of the Götemar pluton in county Blekinge (Figure 1a). They reveal an NW-striking penetrative fabric likely created by NE-SW shortening (Wahlgren & Stephens, 2020). The AMS fabric of plutons commonly reflects the direction of regional shortening if emplaced in a compressional stress field (Burton-Johnson et al., 2019; McCarthy, Reavy, et al., 2015). The Götemar pluton AMS foliations do not show a dominant NW-SE alignment, which suggests that the pluton was not emplaced within a compressional stress field (see Figure 7a). A corresponding back-arc extensional stress field related to the Hallandian Orogen may therefore have controlled the attitude of the NW-SE striking dikes within the Götemar pluton.

The concentric subhorizontal sheet attitudes in the Götemar pluton, on the other hand, suggest a link to the local magmatic stress field. Curved magmatic sheets such as ring-dikes and inclined sheets are common features in the host rock to shallow magmatic systems (Anderson, 1937; Burchardt et al., 2013; Burchardt & Gudmundsson, 2009; Klausen, 2004; Magee et al., 2012; Schirnick et al., 1999). The classic model of ring-dike formation involves the subsidence of a block overlying magma leading to the formation of steeply dipping bell-jar-shaped dikes (Anderson, 1937; Clough et al., 1909). Inclined sheets, on the other hand, dip toward the magmatic source (Anderson, 1937; Jackson et al., 2013; Le Bas, 1971; Phillips, 1974; Planke et al., 2005; Polteau et al., 2008; Schmiedel et al., 2017). The dominantly outward dipping to subhorizontal sheets in the Götemar pluton can neither be described as inclined sheets nor ring dikes (Figure 4a). The viscosities of a magma mush are orders of magnitude higher than the viscosities of a melt-dominated magma and therefore behave as a rigid crystal network when it is deformed (Bergantz et al., 2017; Costa et al., 2009; Marsh, 1996; Petford, 2009; Picard et al., 2013). During the late-stage growth of sub-volcanic laccoliths, deformation of viscous already emplaced magma produces contact parallel strain partitioning features such as banded/layered breccias (Burchardt et al., 2019; Mattsson et al., 2018). The concentric internal features of the Götemar pluton, including the sheet orientations, the medium-grained granite AMS foliations and lineations, and the late-stage deformation zones (Figures 1b, 2, and 7), indicate that new magma intruding the Götemar magma body was accommodated by displacements along localized concentric magmatic shear zones in the viscously stalled mush. Shear zones have been shown to act as magma pumps and drivers of magma migration in orogenic settings (Weinberg et al., 2006). We therefore propose that magma intruding into the mush exploited magma emplacement-related concentric shear zones within the Götemar magma mush to flow laterally in concentrically striking sheets (see Section 5.2 above). Since our mapping identifies several concentrically flowing sheets that are separated by coarse-grained granite and U-shaped internal sheet contacts, we suggest that magma flowed in lobe-like fingers within the magma mush, similar to magma transport in sills (Figures 3i and 8) (cf. Magee et al., 2016; Pollard et al., 1975; Schofield et al., 2012). The change in magma sheet attitude from vertical to subhorizontal along strike shows that the magmatic stress field in the magma body changed from the North to the East away from the feeder to favor subhorizontal magma transport (Figures 2 and 8). Although speculative, the differences in the internal stress field could be related to a trapdoor - style deflection of the magma body roof that opened toward the East-southeast. In this case, trap-door roof deflection prompted the sheets to propagate horizontally in the eastern part of the pluton perpendicular to the easy axes of pluton growth.

The Götemar pluton highlights that (a) the interplay between the magmatic and the regional tectonic stress field is controlling magma transport in magma mush systems and (b) that the magma transport mechanisms in mush systems are similar to transport mechanisms in non-magmatic host rock. Notably, horizontal magmatic sheet propagation is controlled by the emplacement-related structures and stresses within the magma body. Therefore, the magma sheet distribution associated with dominant floor subsidence type pluton emplacement can be expected to yield different magma transport architecture compared to magma bodies that were predominantly emplaced by inflation and roof and wall deflection, such as the Götemar pluton.

6. Conclusions

- The parallel concentrically flowing microgranite and medium-grained granite sheets exposed throughout the circular Götemar pluton show that magma transport is linked to its concentric emplacement-related structure.
- Flow of magma within the magmatic sheets transitioned from vertical in the NW to lateral/horizontal along strike toward the center of the magma body and migrated to the crystal mush in the form of melt fingers.
- NW-SE striking subvertical magmatic sheets indicate an influence of the regional Hallandian orogenic stress field on vertical sheet orientations within the pluton.
- The magmatic sheet architecture of the Götemar pluton shows that it is important to establish the pluton emplacement mechanism to understand the magma transport within magma mush systems.
- The Götemar pluton shows that magma sheet emplacement within mushy magma bodies is strongly influenced by both the local magmatic and the regional stress fields.

Conflict of Interest

The authors declare no conflicts of interest relevant to this study.

Data Availability Statement

All data collected during this study are published in the Swedish National Data Service repository (Mattsson et al., 2023).

Acknowledgments
The authors thank Bjarne Almqvist for access to sampling and sample preparation equipment and Steffi Burchardt for helpful discussions about the study. The authors are grateful to Whitney Behr for editorial handling and Robert Miller and Roberto Weinberg for reviews that greatly improved the quality of the work. The study was funded by the Swedish Research Council Grant (2019-06300) to Tobias Mattsson.

References

Åhäll, K.-I. (2001). Åldersbestämning av svårdaterade bergarter i sydöstra Sverige. SKB R-01-60. Swedish Nuclear Fuel and Waste Management (SKB).

Akimoto, S. (1962). Magnetic properties of FeO-Fe2O3-TiO2 system as a basis of rock magnetism. *Journal of the Physical Society of Japan*, *17*, 706–710.

Allmendinger, R. W., Cardozo, N., & Fisher, D. (2012). *Structural geology algorithms: Vectors and tensors*. Cambridge University Press.

Anderson, E. M. (1937). IX.—The dynamics of the formation of cone-sheets, ring-dykes, and caldron-subsidences. *Proceedings of the Royal Society of Edinburgh*, *56*, 128–157. https://doi.org/10.1017/S0370164600014954

Bartley, J. M., Coleman, D. S., & Glazner, A. F. (2006). Incremental pluton emplacement by magmatic crack-seal. *Transactions of the Royal Society of Edinburgh Earth Sciences*, *97*(4), 383–396. https://doi.org/10.1017/S0263593300001528

Bergantz, G. W., Schleicher, J. M., & Burgisser, A. (2017). On the kinematics and dynamics of crystal-rich systems. *Journal of Geophysical Research: Solid Earth*, *122*(8), 6131–6159. https://doi.org/10.1002/2017JB014218

Biedermann, A. (2018). Magnetic anisotropy in single crystals: A review. *Geosciences*, *8*, 302. https://doi.org/10.3390/geosciences8080302

Bilardello, D. (2020). Practical magnetism II: Humps and a bump, the maghemite song. *The IRM Quarterly*, *30*, 1–17.

Bogdanova, S. V., Čečys, A., Bibikova, E. V., Ilyinsky, L. S., & Taran, L. N. (2014). Danopolonian migmatization of mesoproterozoic sedimentary rocks in southernmost Sweden: A SIMS zircon study. *GFF*, *136*(2), 410–428. https://doi.org/10.1080/11035897.2013.855815

Bogdanova, S. V., Page, L. M., Skridlaite, G., & Taran, L. N. (2001). Proterozoic tectonothermal history in the western part of the East European craton: $^{40}Ar/^{39}Ar$ geochronological constraints. *Tectonophysics*, *339*(1–2), 39–66. https://doi.org/10.1016/S0040-1951(01)00033-6

Borradaile, G. J., & Jackson, M. (2010). Structural geology, petrofabrics and magnetic fabrics (AMS, AARM, AIRM). *Journal of Structural Geology*, *32*(10), 1519–1551. https://doi.org/10.1016/j.jsg.2009.09.006

Brander, L., & Söderlund, U. (2009). Mesoproterozoic (1.47–1.44 Ga) orogenic magmatism in Fennoscandia; Baddeleyite U–Pb dating of a suite of massif-type anorthosite in S. Sweden. *International Journal of Earth Sciences*, *98*(3), 499–516. https://doi.org/10.1007/s00531-007-0281-0

Burchardt, S., & Gudmundsson, A. (2009). The infrastructure of Geitafell volcano, southeast Iceland. In *Studies in volcanology: The legacy of George Walker* (Vol. 2, pp. 349–370). Special Publication of IAVCEI.

Burchardt, S., Mattsson, T., Palma, J. O., Galland, O., Almqvist, B., Mair, K., et al. (2019). Progressive growth of the Cerro Bayo Cryptodome, Chachahuén Volcano, Argentina—Implications for viscous magma emplacement. *Journal of Geophysical Research: Solid Earth*, *124*(8), 7934–7961. https://doi.org/10.1029/2019JB017543

Burchardt, S., Tanner, D., & Krumbholz, M. (2012). The Slaufrudalur pluton, southeast Iceland-An example of shallow magma emplacement by coupled cauldron subsidence and magmatic stoping. *Geological Society of America Bulletin*, *124*(1–2), 213–227. https://doi.org/10.1130/B30430.1

Burchardt, S., Troll, V. R., Mathieu, L., Emeleus, H. C., & Donaldson, C. H. (2013). Ardnamurchan 3D cone-sheet architecture explained by a single elongate magma chamber. *Scientific Reports*, *3*(1), 2891. https://doi.org/10.1038/srep02891

Burton-Johnson, A., Macpherson, C. G., Muraszko, J. R., Harrison, R. J., & Jordan, T. A. (2019). Tectonic strain recorded by magnetic fabrics (AMS) in plutons, including Mt Kinabalu, Borneo: A tool to explore past tectonic regimes and syn-magmatic deformation. *Journal of Structural Geology*, *119*, 50–60. https://doi.org/10.1016/j.jsg.2018.11.014

Cañón-Tapia, E. (2004). Anisotropy of magnetic susceptibility of lava flows and dykes: A historical account. *Geological Society, London, Special Publications*, *238*(1), 205–225. https://doi.org/10.1144/GSL.SP.2004.238.01.14

Cashman, K. V., Sparks, R. S. J., & Blundy, J. D. (2017). Vertically extensive and unstable magmatic systems: A unified view of igneous processes. *Science*, *355*(6331), eaag3055. https://doi.org/10.1126/science.aag3055

Castro, J. M., Dingwell, D. B., Nichols, A. R. L., & Gardner, J. E. (2005). New insights on the origin of flow bands in obsidian. In M. Manga & G. Ventura (Eds.), *Special paper 396: Kinematics and dynamics of lava flows* (pp. 55–65). Geological Society of America. https://doi.org/10.1130/0-8137-2396-5.55

Chadima, M., Cajz, V., & Týcová, P. (2009). On the interpretation of normal and inverse magnetic fabric in dikes: Examples from the Eger Graben, NW Bohemian Massif. *Tectonophysics*, *466*(1–2), 47–63. https://doi.org/10.1016/j.tecto.2008.09.005

Chadima, M., Hrouda, F., & Jelínek, V. (2019). Anisoft5.

Chadima, M., Pokorny, J., & Dusek, M. (2018). Rema6.

Chan, C. F., Shea, E. K., Kent, A. J. R., Miller, R. B., Miller, J. S., & Bowring, S. A. (2017). Formation of a sheeted intrusive complex within the deep-crustal Tenpeak pluton, North Cascades, Washington. *Geosphere*, *13*(5), 1610–1639. https://doi.org/10.1130/GES01323.1

Clemens, J. D., Stevens, G., le Roux, S., & Wallis, G. L. (2020). Mafic schlieren, crystal accumulation and differentiation in granitic magmas: An integrated case study. *Contributions to Mineralogy and Petrology*, *175*(5), 51. https://doi.org/10.1007/s00410-020-01689-x

Clough, C. T., Maufe, H. B., & Bailey, E. B. (1909). The cauldron-subsidence of Glen Coe, and the associated igneous phenomena. *Quarterly Journal of the Geological Society*, *65*(1–4), 611–678. https://doi.org/10.1144/GSL.JGS.1909.065.01-04.35

Costa, A., Caricchi, L., & Bagdassarov, N. (2009). A model for the rheology of particle-bearing suspensions and partially molten rocks. *Geochemistry, Geophysics, Geosystems*, *10*(3), Q03010. https://doi.org/10.1029/2008GC002138

Cruden, A. R. (1998). On the emplacement of tabular granites. *Journal of the Geological Society*, *155*(5), 853–862. https://doi.org/10.1144/gsjgs.155.5.0853

Cruden, A. R. (2008). *Emplacement mechanisms and structural influences of a younger granite intrusion into older wall rock-a principal study with application to the Götemar and Uthammar granites. SKB-R-08-138*. Swedish Nuclear Fuel and Waste Management (SKB).

Cruden, A. R., & McCaffrey, K. J. W. (2001). Growth of plutons by floor subsidence: Implications for rates of emplacement, intrusion spacing and melt-extraction mechanisms. *Physics and Chemistry of the Earth - Part A: Solid Earth and Geodesy*, *26*(4–5), 303–315. https://doi.org/10.1016/S1464-1895(01)00060-6

Drake, H., Tullborg, E.-L., & Page, L. (2009). Distinguished multiple events of fracture mineralisation related to far-field orogenic effects in Paleoproterozoic crystalline rocks, Simpevarp area, SE Sweden. *Lithos*, *110*(1–4), 37–49. https://doi.org/10.1016/j.lithos.2008.12.003

Dunlop, D. J., & Özdemir, Ö. (1997). Rock magnetism. Fundamentals and frontiers, 1998/03/01. In *Cambridge studies in magnetism series XXI*. Cambridge University Press. https://doi.org/10.1017/S0016756898218437

Ferré, E. C. (2002). Theoretical models of intermediate and inverse AMS fabrics. *Geophysical Research Letters*, *29*(7), 1127. https://doi.org/10.1029/2001GL014367

Friese, N., Vollbrecht, A., Tanner, D. C., Fahlbusch, W., & Weidemann, M. (2012). Multi-stage emplacement of the Götemar pluton, SE Sweden: New evidence inferred from field observations and microfabric analysis, including cathodoluminescence microscopy. *International Journal of Earth Sciences*, *101*(5), 1149–1167. https://doi.org/10.1007/s00531-011-0739-y

Gaillot, P., de Saint-Blanquat, M., & Bouchez, J.-L. (2006). Effects of magnetic interactions in anisotropy of magnetic susceptibility: Models, experiments and implications for igneous rock fabrics quantification. *Tectonophysics*, *418*(1–2), 3–19. https://doi.org/10.1016/j.tecto.2005.12.010

Geoffroy, L., Callot, J. P., Aubourg, C., & Moreira, M. (2002). Magnetic and plagioclase linear fabric discrepancy in dykes: A new way to define the flow vector using magnetic foliation. *Terra Nova*, *14*(3), 183–190. https://doi.org/10.1046/j.1365-3121.2002.00412.x

Gilbert, G. K. (1877). *Report on the geology of the Henry mountains*. US Geographical and Geological Survey.

Glazner, A. F. (2021). Thermal constraints on the longevity, depth, and vertical extent of magmatic systems. *Geochemistry, Geophysics, Geosystems*, *22*(4), e2020GC009459. https://doi.org/10.1029/2020GC009459

Gonnermann, H. M., & Manga, M. (2005). Flow banding in obsidian: A record of evolving textural heterogeneity during magma deformation. *Earth and Planetary Science Letters*, *236*(1–2), 135–147. https://doi.org/10.1016/j.epsl.2005.04.031

Grégoire, V., Darrozes, J., Gaillot, P., Nédélec, A., & Launeau, P. (1998). Magnetite grain shape fabric and distribution anisotropy vs rock magnetic fabric: A three-dimensional case study. *Journal of Structural Geology*, *20*(7), 937–944. https://doi.org/10.1016/S0191-8141(98)00022-4

Hargraves, R. B., Johnson, D., & Chan, C. Y. (1991). Distribution anisotropy: The cause of AMS in igneous rocks? *Geophysical Research Letters*, *18*(12), 2193–2196. https://doi.org/10.1029/91GL01777

Harry, W. T., & Richey, J. E. (1963). Magmatic pulses in the emplacement of plutons. *Geological Journal*, *3*(2), 254–268. https://doi.org/10.1002/gj.3350030204

Hawkes, L., & Hawkes, H. K. (1933). The Sandfell laccolith and "dome of elevation.". *Quarterly Journal of the Geological Society*, *89*(1–4), 379–400. https://doi.org/10.1144/GSL.JGS.1933.089.01-04.14

Hext, G. R. (1963). The estimation of second-order tensors, with related tests and designs. *Biometrika*, *50*(3–4), 353–373. https://doi.org/10.1093/biomet/50.3-4.353

Hildebrand, R. S., Hoffman, P. F., Housh, T., & Bowring, S. A. (2010). The nature of volcano-plutonic relations and the shapes of epizonal plutons of continental arcs as revealed in the Great Bear magmatic zone, northwestern Canada. *Geosphere*, *6*, 812–839. https://doi.org/10.1130/GES00533.1

Hrouda, F. (1982). Magnetic anisotropy of rocks and its application in geology and geophysics. *Geophysical Surveys*, *5*(1), 37–82. https://doi.org/10.1007/BF01450244

Hutton, D. H. W. (1988). Granite emplacement mechanisms and tectonic controls: Inferences from deformation studies. *Transactions of the Royal Society of Edinburgh Earth Sciences*, *79*(2–3), 245–255. https://doi.org/10.1017/S0263593300014255

Jackson, C. A.-L., Schofield, N., & Golenkov, B. (2013). Geometry and controls on the development of igneous sill-related forced folds: A 2-D seismic reflection case study from offshore southern Australia. *Geological Society of America Bulletin*, *125*(11–12), 1874–1890. https://doi.org/10.1130/B30833.1

Jackson, M. (1991). Anisotropy of magnetic remanence: A brief review of mineralogical sources, physical origins, and geological applications, and comparison with susceptibility anisotropy. *Pure and Applied Geophysics PAGEOPH*, *136*, 1–28. https://doi.org/10.1007/BF00878885

Jackson, M. D., Blundy, J., & Sparks, R. S. J. (2018). Chemical differentiation, cold storage and remobilization of magma in the Earth's crust. *Nature*, *564*(7736), 405–409. https://doi.org/10.1038/s41586-018-0746-2

Jacques, J. M., & Reavy, R. J. (1994). Caledonian plutonism and major lineaments in the SW Scottish Highlands. *Journal of the Geological Society*, *151*(6), 955–969. https://doi.org/10.1144/gsjgs.151.6.0955

Jelínek, V. (1977). *The statistical theory of measuring anisotropy of magnetic susceptibility of rocks and its application*. Geofyzika.

Jelínek, V. (1978). Statistical processing of anisotropy of magnetic susceptibility measured on groups of specimens. *Studia Geophysica et Geodaetica*, *22*(1), 50–62. https://doi.org/10.1007/BF01613632

Jelínek, V. (1981). Characterization of the magnetic fabric of rocks. *Tectonophysics*, *79*(3–4), T63–T67. https://doi.org/10.1016/0040-1951(81)90110-4

Khan, M. A. (1962). The anisotropy of magnetic susceptibility of some igneous and metamorphic rocks. *Journal of Geophysical Research*, *67*(7), 2873–2885. https://doi.org/10.1029/JZ067i007p02873

Klausen, M. B. (2004). Geometry and mode of emplacement of the Thverartindur cone sheet swarm, SE Iceland. *Journal of Volcanology and Geothermal Research*, *138*(3–4), 185–204. https://doi.org/10.1016/j.jvolgeores.2004.05.022

Knight, M. D., & Walker, G. P. L. (1988). Magma flow directions in dikes of the Koolau Complex, Oahu, determined from magnetic fabric studies. *Journal of Geophysical Research*, *93*(B5), 4301–4319. https://doi.org/10.1029/JB093iB05p04301

Kresten, P., & Chyssler, J. (1976). The Götemar massif in south-eastern Sweden: A reconnaissance survey. *Geologiska Foreningen i Stockholm Forhandlingar*, *98*(2), 155–161. https://doi.org/10.1080/11035897609454357

Lattard, D., Engelmann, R., Kontny, A., & Sauerzapf, U. (2006). Curie temperatures of synthetic titanomagnetites in the Fe-Ti-O system: Effects of composition, crystal chemistry, and thermomagnetic methods. *Journal of Geophysical Research*, *111*(B12), B12S28. https://doi.org/10.1029/2006JB004591

Le Bas, M. J. (1971). Cone-sheets as a mechanism of uplift. *Geological Magazine*, *108*(5), 373–376. https://doi.org/10.1017/S0016756800056399

Liu, Q., Deng, C., Yu, Y., Torrent, J., Jackson, M. J., Banerjee, S. K., & Zhu, R. (2005). Temperature dependence of magnetic susceptibility in an argon environment: Implications for pedogenesis of Chinese loess/palaeosols. *Geophysical Journal International*, *161*(1), 102–112. https://doi.org/10.1111/j.1365-246X.2005.02564.x

London, D. (2009). The origin of primary textures in granitic pegmatites. *The Canadian Mineralogist*, *47*(4), 697–724. https://doi.org/10.3749/canmin.47.4.697

Lowrie, W. (1990). Identification of ferromagnetic minerals in a rock by coercivity and unblocking temperature properties. *Geophysical Research Letters*, *17*(2), 159–162. https://doi.org/10.1029/GL017i002p00159

Lowrie, W., & Fuller, M. (1971). On the alternating field demagnetization characteristics of multidomain thermoremanent magnetization in magnetite. *Journal of Geophysical Research*, *76*(26), 6339–6349. https://doi.org/10.1029/JB076i026p06339

Magee, C., Muirhead, J. D., Karvelas, A., Holford, S. P., Jackson, C. A. L., Bastow, I. D., et al. (2016). Lateral magma flow in mafic sill complexes. *Geosphere*, *12*(3), 809–841. https://doi.org/10.1130/GES01256.1

Magee, C., Stevenson, C. T. E., O'Driscoll, B., Schofield, N. J., & McDermott, K. (2012). An alternative emplacement model for the classic Ardnamurchan cone sheet swarm, NW Scotland, involving lateral magma supply via regional dykes. *Journal of Structural Geology*, *43*, 73–91. https://doi.org/10.1016/j.jsg.2012.08.004

Marsh, B. D. (1996). Solidification fronts and magmatic evolution. *Mineralogical Magazine*, *60*(398), 5–40. https://doi.org/10.1180/minmag.1996.060.398.03

Mattsson, T., Burchardt, S., Almqvist, B. S. G., & Ronchin, E. (2018). Syn-emplacement fracturing in the sandfell laccolith, eastern Iceland—Implications for rhyolite intrusion growth and volcanic hazards. *Frontiers in Earth Science*, *6*, 5. https://doi.org/10.3389/feart.2018.00005

Mattsson, T., Burchardt, S., Mair, K., & Place, J. (2020). Trap-door floor subsidence emplacement of the Mourne mountains granite pluton: Insights from the regional fracture pattern. *Journal of Structural Geology*, *16*(1), 182–209. https://doi.org/10.1130/GES02148.1

Mattsson, T., McCarthy, W., & Schmiedel, T. (2023). Data from: Transport of Magma in Granitic Mush Systems; an Example From the Götemar Pluton, Sweden [Dataset]. Stockholm University. https://doi.org/10.58141/3w7y-3n17

Mattsson, T., Petri, B., Almqvist, B., McCarthy, W., Burchardt, S., Palma, J. O., et al. (2021). Decrypting magnetic fabrics (AMS, AARM, AIRM) through the analysis of mineral shape fabrics and distribution anisotropy. *Journal of Geophysical Research: Solid Earth*, *126*(6), e2021JB021895. https://doi.org/10.1029/2021JB021895

McCabe, C., Jackson, M., & Ellwood, B. B. (1985). Magnetic anisotropy in the Trenton Limestone: Results of a new technique, anisotropy of anhysteretic susceptibility. *Geophysical Research Letters*, *12*(6), 333–336. https://doi.org/10.1029/GL012i006p00333

McCarthy, A., & Müntener, O. (2016). Comb layering monitors decompressing and fractionating hydrous mafic magmas in subvolcanic plumbing systems (Fisher Lake, Sierra Nevada, USA). *Journal of Geophysical Research: Solid Earth*, *121*(12), 8595–8621. https://doi.org/10.1002/2016JB013489

McCarthy, W., Petronis, M. S., Reavy, R. J., & Stevenson, C. T. E. (2015). Distinguishing diapirs from inflated plutons: An integrated rock magnetic fabric and structural study on the Roundstone pluton, western Ireland. *Journal of the Geological Society*, *172*(5), 550–565. https://doi.org/10.1144/jgs2014-067

McCarthy, W., Reavy, R. J., Stevenson, C. T., & Petronis, M. S. (2015). Late Caledonian transpression and the structural controls on pluton construction; new insights from the Omey Pluton, western Ireland. *Earth and Environmental Science Transactions of the Royal Society of Edinburgh*, *106*(1), 11–28. https://doi.org/10.1017/S1755691015000201

McNulty, B. A., Tong, W., & Tobisch, O. T. (1996). Assembly of a dike-fed magma chamber: The Jackass Lakes pluton, central Sierra Nevada, California. *Geological Society of America Bulletin*, *108*(8), 926–940. https://doi.org/10.1130/0016-7606(1996)108<0926:AOADFM>2.3.CO;2

Michel, J., Baumgartner, L., Putlitz, B., Schaltegger, U., & Ovtcharova, M. (2008). Incremental growth of the Patagonian Torres del Paine laccolith over 90 k.y. *Geology*, *36*(6), 459. https://doi.org/10.1130/G24546A.1

Miller, R. B., DeBari, S. M., & Paterson, S. R. (2018). Construction, emplacement, and geochemical evolution of deep-crustal intrusions: Tenpeak and Dirtyface plutons, North Cascades, western North America. *Geosphere*, *14*(3), 1298–1323. https://doi.org/10.1130/GES01490.1

Miller, R. B., & Paterson, S. R. (2001). Construction of mid-crustal sheeted plutons: Examples from the North Cascades, Washington. *Geological Society of America Bulletin*, *113*(11), 1423–1442. https://doi.org/10.1130/0016-7606(2001)113<1423:COMCSP>2.0.CO;2

Olivier, P., Druguet, E., Castaño, L. M., & Gleizes, G. (2016). Granitoid emplacement by multiple sheeting during Variscan dextral transpression: The Saint-Laurent—La Jonquera pluton (Eastern Pyrenees). *Journal of Structural Geology*, *82*, 80–92. https://doi.org/10.1016/j.jsg.2015.10.006

Özdemir, Ö., Dunlop, D. J., & Moskowitz, B. M. (1993). The effect of oxidation on the Verwey transition in magnetite. *Geophysical Research Letters*, *20*(16), 1671–1674. https://doi.org/10.1029/93GL01483

Paterson, S. R., & Fowler, T. K. K. (1993). Re-examining pluton emplacement processes. *Journal of Structural Geology*, *15*(2), 191–206. https://doi.org/10.1016/0191-8141(93)90095-R

Petford, N. (2009). Which effective viscosity? *Mineralogical Magazine*, *73*(2), 167–191. https://doi.org/10.1180/minmag.2009.073.2.167

Petronis, M. S., O'Driscoll, B., & Lindline, J. (2011). Late stage oxide growth associated with hydrothermal alteration of the Western Granite, Isle of Rum, NW Scotland. *Geochemistry, Geophysics, Geosystems*, *12*(1), Q01001. https://doi.org/10.1029/2010GC003246

Petronis, M. S., O'Driscoll, B., Stevenson, C. T. E., & Reavy, R. J. (2012). Controls on emplacement of the Caledonian Ross of Mull Granite, NW Scotland: Anisotropy of magnetic susceptibility and magmatic and regional structures. *Geological Society of America Bulletin*, *124*(5–6), 906–927. https://doi.org/10.1130/B30362.1

Phillips, W. J. (1974). The dynamic emplacement of cone sheets. *Tectonophysics*, *24*(1–2), 69–84. https://doi.org/10.1016/0040-1951(74)90130-9

Picard, D., Arbaret, L., Pichavant, M., Champallier, R., & Launeau, P. (2013). The rheological transition in plagioclase-bearing magmas. *Journal of Geophysical Research: Solid Earth*, *118*(4), 1363–1377. https://doi.org/10.1002/jgrb.50091

Pignotta, G. S., Paterson, S. R., Coyne, C. C., Anderson, J. L., & Onezime, J. (2010). Processes involved during incremental growth of the Jackass Lakes pluton, central Sierra Nevada batholith. *Geosphere*, *6*(2), 130–159. https://doi.org/10.1130/GES00224.1

Planke, S., Rasmussen, T., Rey, S. S., & Myklebust, R. (2005). Seismic characteristics and distribution of volcanic intrusions and hydrothermal vent complexes in the Vøring and Møre basins. *Geological Society, London, Petroleum Geology Conference Series*, *6*(1), 833–844. https://doi.org/10.1144/0060833

Pollard, D. D., & Johnson, A. M. (1973). Mechanics of growth of some laccolithic intrusions in the Henry Mountains, Utah, II: Bending and failure of overburden layers and sill formation. *Tectonophysics*, *18*(3–4), 311–354. https://doi.org/10.1016/0040-1951(73)90051-6

Pollard, D. D., Muller, O. H., & Dockstader, D. R. (1975). The form and growth of fingered sheet intrusions. *Geological Society of America Bulletin*, *86*(3), 351. https://doi.org/10.1130/0016-7606(1975)86<351:TFAGOF>2.0.CO;2

Polteau, S., Mazzini, A., Galland, O., Planke, S., & Malthe-Sørenssen, A. (2008). Saucer-shaped intrusions: Occurrences, emplacement and implications. *Earth and Planetary Science Letters*, *266*(1–2), 195–204. https://doi.org/10.1016/j.epsl.2007.11.015

Reichardt, H., & Weinberg, R. F. (2012). The dike swarm of the Karakoram shear zone, Ladakh, NW India: Linking granite source to batholith. *Geological Society of America Bulletin*, *124*(1–2), 89–103. https://doi.org/10.1130/B30394.1

Richey, J. E. (1928). The structural relations of the Mourne granites, Northern Ireland. *Quarterly Journal of the Geological Society*, *83*(1–5), 653. https://doi.org/10.1144/GSL.JGS.1927.083.01-05.27

Ripa, M., & Stephens, M. B. (2020). Chapter 10 Magmatism (1.6–1.4 Ga) and Mesoproterozoic sedimentation related to intracratonic rifting coeval with distal accretionary orogenesis. *Geological Society, London, Memoirs*, *50*(1), 269–288. https://doi.org/10.1144/M50-2017-4

Rocher, S., Alasino, P. H., Larrovere, M. A., Macchioli Grande, M., Moreno, J. A., Dahlquist, J. A., & Morales Cámera, M. M. (2021). Sheeted intrusion of granitic magmas in the upper crust—Emplacement and thermal evolution of the Guandacolinos pluton, NW Argentina. *Tectonophysics*, *816*, 229034. https://doi.org/10.1016/j.tecto.2021.229034

Rochette, P., Aubourg, C., & Perrin, M. (1999). Is this magnetic fabric normal? A review and case studies in volcanic formations. *Tectonophysics*, *307*(1–2), 219–234. https://doi.org/10.1016/S0040-1951(99)00127-4

Scherman, S. (1978). *Förarbeten för platsval, berggrundsundersökningar. KBS Teknisk Rapport 60*. Sveriges Geologiska Undersökning (SGU).

Schirnick, C., Van Den Bogaard, P., & Schmincke, H. U. (1999). Cone sheet formation and intrusive growth of an oceanic island-the Miocene Tejeda complex on Gran Canaria (Canary Islands). *Geology*, *27*(3), 207–210. https://doi.org/10.1130/0091-7613(1999)027<0207:CSFAIG>2.3.CO;2

Schmiedel, T., Burchardt, S., Mattsson, T., Guldstrand, F., Galland, O., Palma, J., & Skogby, H. (2021). Emplacement and segment geometry of large, high-viscosity magmatic sheets. *Minerals*, *11*(10), 1113. https://doi.org/10.3390/min11101113

Schmiedel, T., Kjoberg, S., Planke, S., Magee, C., Galland, O., Schofield, N., et al. (2017). Mechanisms of overburden deformation associated with the emplacement of the Tulipan sill, mid-Norwegian margin. *Interpretation*, *5*(3), SK23–SK38. https://doi.org/10.1190/INT-2016-0155.1

Schofield, N. J., Brown, D. J., Magee, C., & Stevenson, C. T. (2012). Sill morphology and comparison of brittle and non-brittle emplacement mechanisms. *Journal of the Geological Society*, *169*(2), 127–141. https://doi.org/10.1144/0016-76492011-078

Söderlund, P., Page, L. M., & Söderlund, U. (2008). ^{40}Ar–^{39}Ar biotite and hornblende geochronology from the Oskarshamn area, SE Sweden: Discerning multiple proterozoic tectonothermal events. *Geological Magazine*, *145*(6), 790–799. https://doi.org/10.1017/S0016756808005001

Stephenson, A. (1994). Distribution anisotropy: Two simple models for magnetic lineation and foliation. *Physics of the Earth and Planetary Interiors*, *82*(1), 49–53. https://doi.org/10.1016/0031-9201(94)90101-5

Tarling, D. H., & Hrouda, F. (1993). *The magnetic anisotropy of rocks*. Chapman and Hall.

Tauxe, L., Banerjee, S. K., Butler, R. F., & van der Voo, R. (2018). Essentials of paleomagnetism (5th web ed.).

Tillberg, M., Maskenskaya, O. M., Drake, H., Hogmalm, J. K., Broman, C., Fallick, A. E., & Åström, M. E. (2019). Fractionation of rare Earth elements in greisen and hydrothermal veins related to A-type magmatism. *Geofluids*, *2019*, 1–20. https://doi.org/10.1155/2019/4523214

Tuffen, H., Dingwell, D. B., & Pinkerton, H. (2003). Repeated fracture and healing of silicic magma generate flow banding and earthquakes? *Geology*, *31*(12), 1089. https://doi.org/10.1130/G19777.1

Ulmius, J., Andersson, J., & Möller, C. (2015). Hallandian 1.45Ga high-temperature metamorphism in Baltica: P–T evolution and SIMS U–Pb zircon ages of aluminous gneisses, SW Sweden. *Precambrian Research*, *265*, 10–39. https://doi.org/10.1016/j.precamres.2015.04.004

Vigneresse, J. L. (1995). Control of granite emplacement by regional deformation. *Tectonophysics*, *249*(3–4), 173–186. https://doi.org/10.1016/0040-1951(95)00004-7

Wahlgren, C.-H., & Stephens, M. B. (2020). *Chapter 11 Reworking of older (1.8 Ga) continental crust by Mesoproterozoic (1.5–1.4 Ga) orogeny, Blekinge–Bornholm orogen, southeastern Sweden* (Vol. 50, pp. 291–312). Geological Society, London, Memoirs. https://doi.org/10.1144/M50-2017-1

Weinberg, R. F., Mark, G., & Reichardt, H. (2006). Magma ponding in the Karakoram shear zone, Ladakh, NW India. *Geological Society of America Bulletin preprint*, *1*(2008), 1. https://doi.org/10.1130/B26358.1

Weinberg, R. F., & Searle, M. P. (1998). The Pangong injection complex, Indian Karakoram: A case of pervasive granite flowthrough hot viscous crust. *Journal of the Geological Society*, *155*(5), 883–891. https://doi.org/10.1144/gsjgs.155.5.0883

Weinberg, R. F., Sial, A. N., & Mariano, G. (2004). Close spatial relationship between plutons and shear zones. *Geology*, *32*(5), 377–380. https://doi.org/10.1130/G20290.1

Weinberg, R. F., Vernon, R. H., & Schmeling, H. (2021). Processes in mushes and their role in the differentiation of granitic rocks. *Earth-Science Reviews*, *220*, 103665. https://doi.org/10.1016/j.earscirev.2021.103665

Wik, N.-G., Bergström, U., Bruun, Å., Claeson, D., Jelinek, C., Juhojunti, N., et al. (2005). *Beskrivning till regional berggrundskarta över Kalmar län, Ba66*. Sveriges Geologiska Undersökning (SGU).